Asian Journal of Chemistry; Vol. 34, No. 6 (2022), 1537-1542

ASIAN JOURNAL OF CHEMISTRY

https://doi.org/10.14233/ajchem.2022.23713

Photoelectrochemical Efficiency Applications of Antimony-doped Tin Oxide Thin Film by Thermal Evaporation Technique

P. Mohamed Anwar[1], S. Muruganantham[2,*], M. Ismail Fathima[3], A. Ayeshamariam[4,*], S. Beer Mohamed[5], M. Benhaliliba[6,7] and K. Kaviyarasu[8,9]

[1]Department of Physics, Jamal Mohamed College (Autonomous), (Affiliated to Bharathidasan University), Thiruchirappalli-620 020, India
[2]Department of Physics, National College (Autonomous), (Affiliated to Bharathidasan University), Thiruchirappalli-620001, India
[3]Department of Physics, Mangayarkarasi College of Arts and Science for Women (Affiliated to Madurai Kamaraj University), Paravai, Kanmai-625402, India
[4]Department of Physics, Khadir Mohideen College (Affiliated to Bharathidasan University, Thiruchirappalli), Adirampattinam-614701, India
[5]Department of Material Science, Central University of Tamil Nadu, Thiruvarur-610001, India
[6]Film Device Fabrication Characterization and Application FDFCA Research Group, USTOMB, 31130 Oran, Algeria
[7]Physics Faculty, USTOMB University POBOX 1505 31130, Mnaouer Oran, Algeria
[8]UNESCO-UNISA Africa Chair in Nanoscience's Nanotechnology Laboratories, College of Graduate Studies, University of South Africa (UNISA), Muckleneuk Ridge, P.O. Box 392, Pretoria, South Africa
[9]Nanosciences African network (NANOAFNET), Materials Research Group (MRG), iThemba LABS-National Research Foundation (NRF), 1 Old Faure Road, 7129, P O Box 722, Somerset West, Western Cape Province, South Africa

*Corresponding author: E-mail: ayeshamariamkmc@gmail.com

Received: 4 January 2022; *Accepted*: 19 March 2022; *Published online*: 18 May 2022; AJC-20819

Antimony-doped tin oxide (ATO) Sb–SnO_2 has been prepared by thermal evaporation technique on indium tin oxide (ITO) glass substrate. The prepared ATO thin film was characterized by X-ray diffraction technique (XRD), scanning electron microscope (SEM), energy-dispersive X-ray spectroscopy (EDAX), UV-vis's spectrometer, Fourier transform infrared spectroscopy (FTIR) and photoluminescence studies (PLS) at room temperature, 250 and 500 ºC. Furthermore, the as-fabricated ATO/indium tin oxide device was subjected to electrical measurements, was determined at room temperature and 500 ºC without etching, chemical etching and photoetching processes. Post-treatment, such as annealing and etching, electrochemical photocurrent results showed that the maximum photoelectrochemical performance without etching at 500 ºC of the PEC cell.

Keywords: Photoelectrochemical Efficiency, Antimony, Tin oxide, Thin film, Thermal evaporation technique.

INTRODUCTION

Tin oxide (SnO_2) is a semiconductor with a band gap of 3.6 eV. The oxygen vacancies, formed by the transfer of an oxygen atom of a normal site in the tin gaseous state, are used to obtain an n-type semiconductor. In fact, the free electrons will bind to Sn^{4+} tin atoms, converting them to Sn^{2+} and acting as electron donors. Many gases' adsorption is normally reversible at temperatures between 400 and 500 ºC. For this, SnO_2 material is usually used in the field of monitoring air pollution and toxic gas detection [1].

The most widely observed transparent conductors are doped/undoped stoichiometric/sub-stoichiometric oxides of tin, indium, cadmium and zinc, as well as their alloys. As a result, the doping process, in which an appropriate dopant is applied to SnO_2 to maximize carrier concentration, is preferred. It was found that indium [2] and fluorine are more effective than other dopants in improving the n-type conductivity of SnO_2 thin films. Indium, on the other hand, is expensive and its price has risen steadily over time, restricting its use in industrial applications [3].

Transparent electrodes, gas meters, static electric charge shields and soft-touch screen controls have all been used for antimony-doped tin dioxide (ATO) thin films [3]. Many properties of tin dioxide semiconductor are considered to be improved and modulated by antimony, allowing it to be used

in a number of applications. The Sb-doped SnO_2 films are used in transparent conducting electrodes (TCO), soft touch screen sensors and static electric charge shielders [4]. More adsorption areas are created when antimony is added to a structure's surface, resulting in a significant increase in the actual surface region [5].

In rechargeable Li batteries and optical electronic devices, doping SnO_2 with Sb, Mo and F is common. Antimony is the perfect dopant for SnO_2 because after it is doped with Sb, SnO_2 has preferable conductivity and clarity in visible light wavelengths. As antimony is doped into SnO_2, oxygen vacancies form at the grain boundary layer, lowering the potential barrier and increasing charge carrier mobility [6]. The solvothermal route was used to make Sb-doped SnO_2 nanoparticles at various temperatures, beginning with $SnCl_4{\cdot}5H_2O$ and $SbCl_3$. At 160 ºC, the samples had the lowest resistivity. In the particle size range of 8-15 nm, the powder was monodispersed. The conductivity and optical non-linearity of Sb-doped SnO_2 films on SiO_2 substrate were investigated by Wang *et al.* [7].

The UV photoluminescence (PL) emitted by SnO_2–Sb thin films at various temperatures was studied by Wang *et al*. [8]. RF magnetron sputtering techniques were used to make ATO thin films on glass substrates. With an increase in oxygen partial pressure and a drop in environmental temperature, the intensity of the photoluminescence peak rises dramatically. The donor acceptor band transition from Sb doping is responsible for the observed room-temperature UV emission. The photoelectrochemical (PEC) studies on spray-deposited n-Sb_2S_3 thin film/polyiodide/C PEC solar cells were recorded by Rajpure *et al*. [9]. The Sb_2S_3 thin films are n-type conductivity, as determined by spectral response, photo response and photovoltaic rise and decay. The cell's fill factor and efficiency were both estimated at 59.5% and 0.30%, respectively. It was concluded that the annealing and etching enhanced the PEC cell's efficiency.

The synthesis and electrical properties of ATO powders with barite matrix were reported by Hu *et al*. [10]. The Sb–SnO_2/barite (SSB) composite conductive powders were made by depositing ATO nanoparticles on barite. The influence of oxygen accumulation also on characteristics of sputtered SnO_2–Sb thin films at low temperature have been examined by Lee [11]. It was investigated if multi-walled carbon nanotubes (MWCNTs) distributed in surfactants can be used as adjacent conductive elements in an ATO matrix. Low MWCNT concentrations are essential to minimize the resistivity of conducting ATO films by a factor of 16 while ensuring 90% transparency in the visible region [12].

Coleman *et al*. [13] used a sequential preparation approach to investigate the electrochromic properties of nanoparticulate-doped metal oxides, as well as their optical and material properties. On ATO and nickel-doped tin oxide electrodes, Wong *et al*. [14] recorded the electrolytic ozone production. Ozone was created with high efficiency in perchloric acid as an anode coated with ATO, according to a recent report. The best Ni:Sb:Sn ratio was found to be 1:8:500, which resulted in an ozone production current efficiency of over 30% at room temperature.

In this article, we concentrate on Sb doped SnO_2 thin films prepared on the ITO glass substrates using a thermal evaporation technique which is quick, convenient and low-cost. The Structure, optical and electrochemical properties of the samples were determined and a simple method for performing FTIR measurements on thin oxide films was proposed. The effect of antimony inclusion on the photoelectrochemical current generation has received special attention.

EXPERIMENTAL

Sb-doped SnO_2 powder preparation: Antimony-doped tin oxide (ATO) was used as a phenol oxidation catalyst, conductive transparent optical thin film, electrochromic materials for printed screens, hazardous waste control and heat shields, among other things. To increase the catalytic properties of ATO nanoparticles synthesized by co-precipitation, the particle size must be decreased. Co-precipitation is a cost-efficient preparation method that forms homogeneous solutions that contain metallic sources. The $SnCl_2{\cdot}2H_2O$ (25 g) and $SbCl_3$ (0.5 g) were dissolved in 500 mL of deionized water and stirred the mixture using a magnetic stirrer for 45 min at 60 ºC. Then, 20 mL of acetylacetone and 80 mL of methanol were added to the above solution dropwise for 45 min and stirred the solution for 0.5 h. Finally, ammonia solution was added to the solution dropwise. After a precipitate had formed, the solution was kept in a cool water bath for 24 h, then washed with deionized water several times to remove Cl^- ions and kept at 80 ºC for 4 h [15].

Thin film deposition

Thermal evaporation technique: The temperature of the substrate during deposition plays an important role in determining film structure. The evaporation method is preferred over the sputtering method due to the greater control of the experimental conditions [16].

The molybdenum boat was fixed in between the copper electrode plates and a pellet form of Sb-doped SnO_2 with a thickness of 300 nm was inserted in it. The distance between the indium tin oxide (ITO) substrate and the electrode was 6.5 cm. Air circulation was arranged using a diffusion pump to prevent overheating the chamber. The temperature of the sample was gradually raised by gradually increasing the electrode voltage (10-120 V). The time allowed for deposition was up to 20 min. The vacuum chamber's working pressure was between 1105 and 5105 mbar [17].

After the ATO thin film preparation the crystalline structure, lattice parameter and crystallite size were characterized by X-ray diffraction (XRD) was carried out on a Siemens D-5000 instrument, equipped with LiF (100) monochromator and Cu$K\alpha$ radiation and crystallite size measurements were carried, considering the Scherrer's equation. The ATO thin film morphological surface was studied by scanning electron microscopy (SEM). The presence of functional groups elements were studied Shimadzu FTIR spectrometer in 1200-400 cm^{-1} region. A UV-Vis was used to measure optical transmittance in the wavelength range 200-2400 nm with respect to the normal of the sample. The photoluminescence intensity was measured by photoluminescence studies. The electrochemical measurements (electrochemical impedances spectroscopy and electro-

chemical photocurrent) were performed using an Autolab PGSTAT302 N Galvanostat-Potentiostat equipped with a Frequency Analyzer Module.

RESULTS AND DISCUSSION

XRD pattern analysis: The XRD patterns of the co-precipitated ATO powders calcined at different temperatures such as room temperature, 250 and 500 ºC for 4 h in atmospheric condition are displayed in Fig. 1. The observed *d* values are in good agreement with the standard *d* values (JCPDS Card No. 88-0287) and confirmed the polycrystalline tetragonal structure of the ATO nanopowder [18]. The samples were oriented strongly along the (110) plane. Other reflections were observed along the (101), (200), (211), (220), (002), (310), (112), (310) and (321) planes. As the calcination temperature goes up, grain growth accelerated. The increase in crystallinity as calcination temperature rises is due to an adequate increase in thermal energy supply for grain crystallization, re-crystallization and expansion. It is found that as the annealing temperature rises, crystallinity rises as well (Table-1).

Crystallite size was calculated using Scherrer's formula:

$$D = \frac{0.9\times\lambda}{\beta\times\cos\theta} \quad (1)$$

where D is the crystallite size, β is the broadening of the diffraction line measured at half the maximum intensity and λ is the X-ray wavelength (1.5406 Å).

The XRD patterns show that the intensity of the diffraction peaks increased and the full-width half maximum decreased with the rise in calcination temperature. This result is owed to the difference in the arrangement tropism of the cells in the ultrafine powder, especially the odorless arrangement of atoms in the crystal surfaces and grain interfaces. A considerable amount of oxygen vacancy occurs in the ultrafine powder along with tiny strains during the preparation of the powders in the case of crystal lattice defect.

Therefore, the strain ε in the samples was determined using the following equation [19]:

$$\beta\cos\frac{\theta}{\lambda} = \frac{1}{\varepsilon} + \eta\sin\frac{\theta}{\lambda} \quad (2)$$

where η and ε are the effective particle size and effective strain, respectively. The effective particle size was estimated by plotting βcos θ/λ *versus* sin θ/λ. The calculated values of the lattice parameters, cell volume, effective particle size and effective strain were tabulated.

SEM and EDAX analysis: The SEM analysis is used to analyse the surface morphological structure of ATO thin film by thermal evaporation process. Fig. 2a-c show the SEM images of the prepared ATO nano powders at room temperature and calcined 500 ºC for 4 h in air atmospheric condition.

The calcined powder has a high degree of agglomeration and the grain size distribution of its nanorod-like features ranges from nano size to a few microns in axial length. Fig. 2c exhibited the axial length and sectional diameters slightly improved after annealing at 500 ºC. This observation supports the XRD results [20]. The EDX analysis shows the chemical composition of Sb-SnO_2 sample. The concentration of Sb in

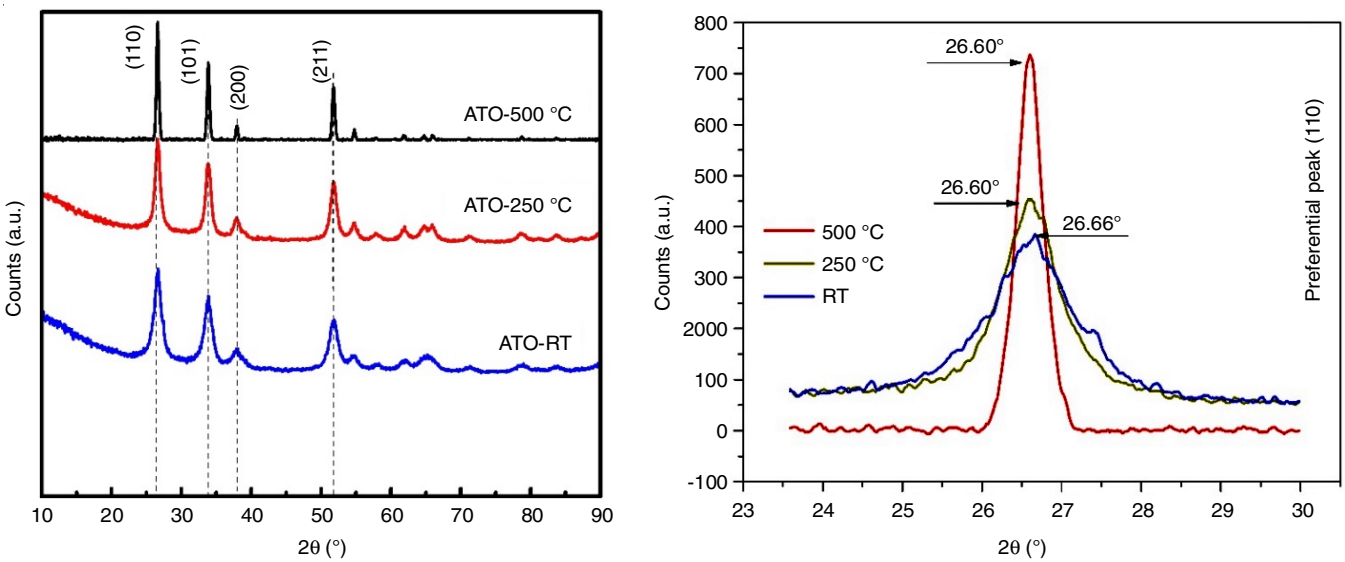

Fig. 1. XRD pattern showing the preferential peak position (110) shift *vs*. different temperatures of the ATO thin film by thermal evaporation process

TABLE-1
STRUCTURAL PARAMETERS CALCULATED USING X-RAY PATTERN RESULTS

Calcination temperature (°C)	Lattice parameters (Å)		Cell volume (Å)^3	Effective particle size (nm)	Crystallite size (Å)	Effective strain (× 10^{-2})
	a	c				
Room temp.	4.73	3.19	71.60	25.3	37.5	1.0
250	4.72	3.20	71.70	10.3	14.3	1.4
500	4.74	3.18	71.40	9.6	13.0	9

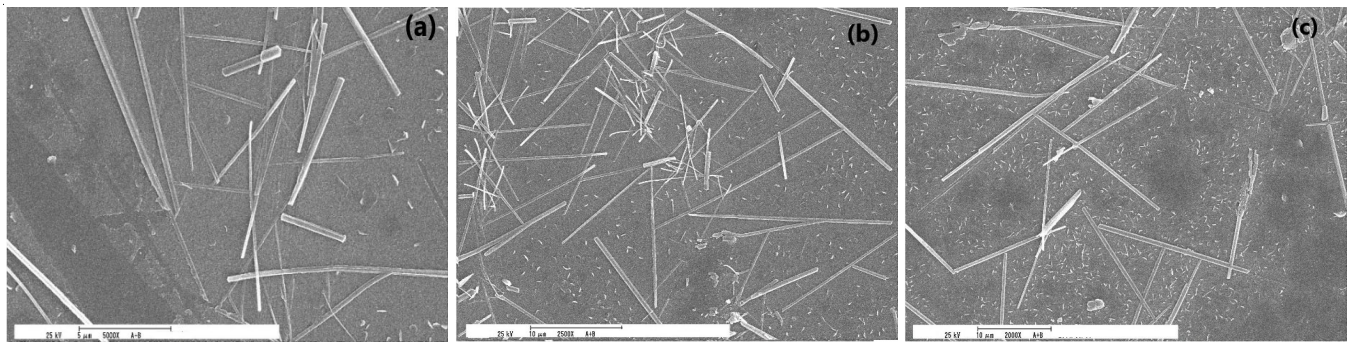

Fig. 2. SEM images of ATO nano powders (a) room temperature (b) 250 °C and (c) 500 °C

the SnO_2 crystal is 23.45% as described at 500 ºC as shown in Table-2. The peak broadening pattern in the corresponding EDAX spectrum (Fig. 3) clearly shows that the minimal nanocrystals are present in the samples. The surface morphology of the grains is uniform due to their thinness, resulting in a crystallographic composition of Sb-SnO_2 with microstructure of closed-packed crystallites with nano rod structure changes an excellent stoichiometric surface distribution. As the annealing time is increased, the microstructure of closed packed crystallites with nano structure changes.

TABLE-2
EDAX OF THE ATO CALCINED AT 500 °C

Element	Net counts	Weight (%)	Atom (%)
Sn	7230	23.45	70.13
O	101483	60.56	24.41
Sb	15678	15.99	5.46
Total		100.00	100.00

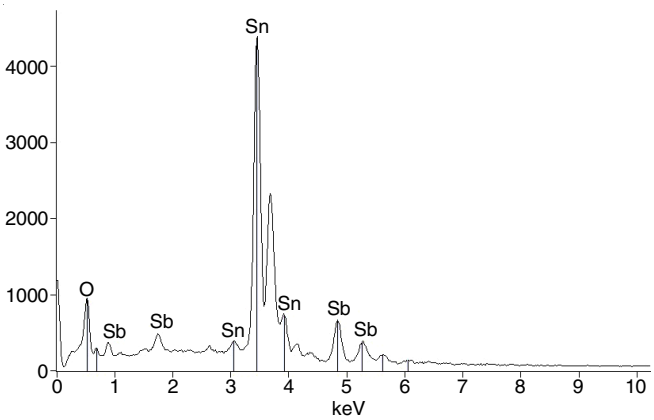

Fig. 3. EDAX scheme of the ATO at room temperature

FTIR studies: Fig. 4 displays the FTIR spectra of ATO nanopowders prepared by co-precipitation at room temperature, 250 ºC and 500 ºC for 4 h in an air atmosphere. The antisymmetric Sn–O–Sn stretching mode of the surface-bridging oxide produced by condensation of adjacent surface hydroxyl groups is correlated with the sharp absorbance peak at 592 cm^{-1} in the fingerprint area. The calcinated powders of Sb-doped SnO_2 have a strong absorption band between 3600 and 3300 cm^{-1}, a weak sharp absorption band between 1630 and 1640 cm^{-1} and a very weak absorption band between 2424 and 2434 cm^{-1}. The hydroxyl groups of physisorbed water molecules bound

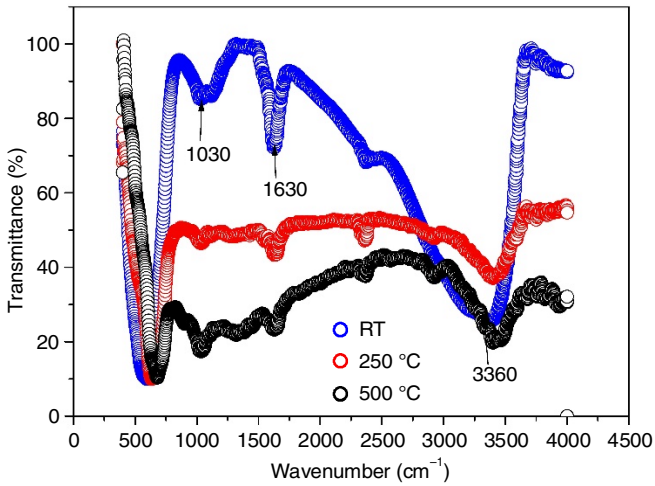

Fig. 4. FTIR spectra of the ATO thin films by thermal evaporation process

to the OH– groups of SnO_2 surfaces by weak hydrogen bonds are characterized by an absorption peak at 3600-3300 cm^{-1} [21]. The deformation vibration of H–O–H bonds in the physiosorbed water is consistent with the slow adsorption at 1630 cm^{-1}. The stretching vibration of the interaction hydroxyl groups, which form hydrogen bonds, is responsible for the weak adsorption band at 2424 cm^{-1} [22].

Optical measurements: The optical measurements can accurately identify the peak location of semiconductor nanostructures' absorption bands, precise determination of their band gap energies (E_g) is difficult. Using the Kubelka–Munk (K-M) equation, the diffuse reflectance spectra of such powdered nanostructures can be used to remove their E_g unambiguously.

Kubelka & Munk [23] suggested the principle that allowed diffuse reflectance spectra to be used. Originally, they suggested a model based on the following differential equations to explain the action of light passing within a light-scattering specimen.

$$-d_i = (S + K)i dx + S_j dx$$

$$d_j = -(S + K)\, j dx + S_i dx$$

where i and j are the intensities of light passing through the sample to its unlit and lit surfaces, respectively; dx is the differential section along the light path; and S and K are the so-called K-M scattering and absorption coefficients, respectively. Even if they tend to reflect portions of light dispersed and absorbed per unit vertical range, these last two quantities

have no clear physical significance on their own [24]. When the particle size is equal to or smaller than the wavelength of the incident light, this model states that diffuse reflection can no longer distinguish the contributions of reflection, refraction and diffraction (*i.e.* scattering occurs).

Kubelka-Munk equation at any wavelength becomes:

$$\frac{k}{s} = \frac{(1-R_\alpha)^2}{2R_\alpha} = F(R_\alpha) \quad (3)$$

where R_α is the diffuse reflectance, k is the absorption coefficient, and s is the scattering coefficient.

The ATO powders' optical band gaps ranged from 3.84 to 4.40 eV. With the rise in annealing temperature, the optical band differences migrated toward higher frequency or lower energies. As a result, it is concluded that as particle size increases, the optical band gap energy decreases against the bulk value of tin oxide (3.60 eV) [25]. Fig. 5 exhibits the prominent peaks with low-intensity tails on the higher side. The emission peaks are located at 362, 426 and 486 nm. Nanostructured materials have more crystalline defects, such as stacking faults and point defects, than their bulk counterparts. These intrinsic defects often cause PL emission at room temperature. In this case, the main UV emission peak at about 362 nm originated from the recombination of free excitons through an exciton-exciton process [26].

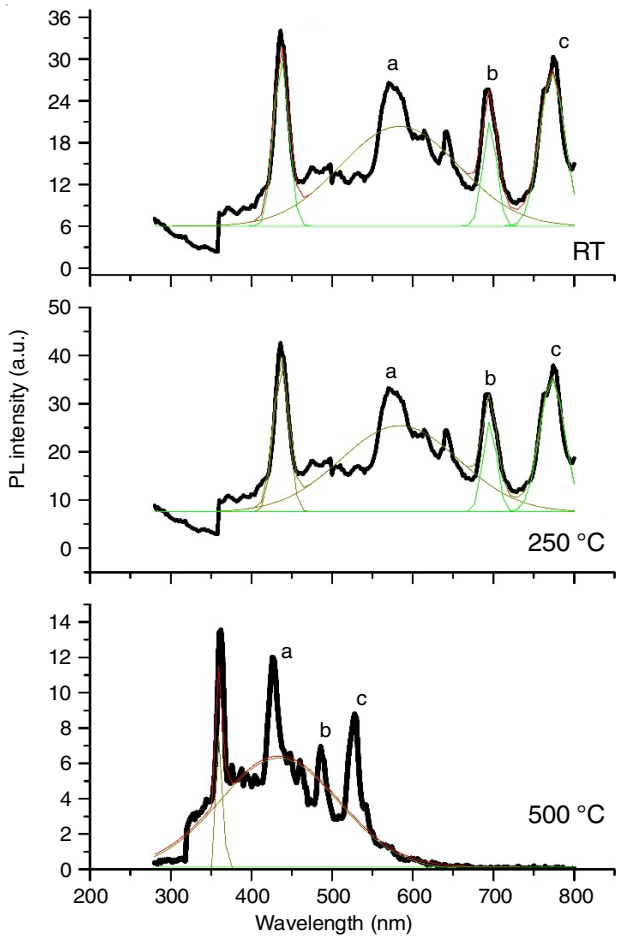

Fig. 5. PL spectrum of the ATO nanopowder with various temperature. The deconvolution profile was sketched for the four main peaks

The second prominent peak at 426 nm and another visible peak at 527 nm for ATO may be related to crystal defects, which formed during the growth of crystallites in calcination processes [10,27]. The emission peak at 486 nm corresponds to green luminescence and can be attributed to singly charged oxygen vacancies in the material [26,28]. The UV emission peak that originated at 362 nm indicates the suitable optical property of ATO as a transparent conducting oxide (TCO) material [29,30].

PEC parameters of Sb-doped SnO_2 thin film photocathodes: The I-V analysis of the best PEC cells using electrodeposited and brush-plated Sb-doped SnO_2 thinfilm, without etching was carried out. A computer simulated program was developed to extract the PEC parameters and compare the experimentally observed data [31]. The PEC parameters of the Sb-doped SnO_2 thin film are presented in Table-3. Fig. 6 shows the short circuit current (J_{sc}) and open circuit voltage (V_{oc}) were calculated from Autolab PGSTAT302 N Galvanostat-Potentiostat equipped with a frequency analyzer module.

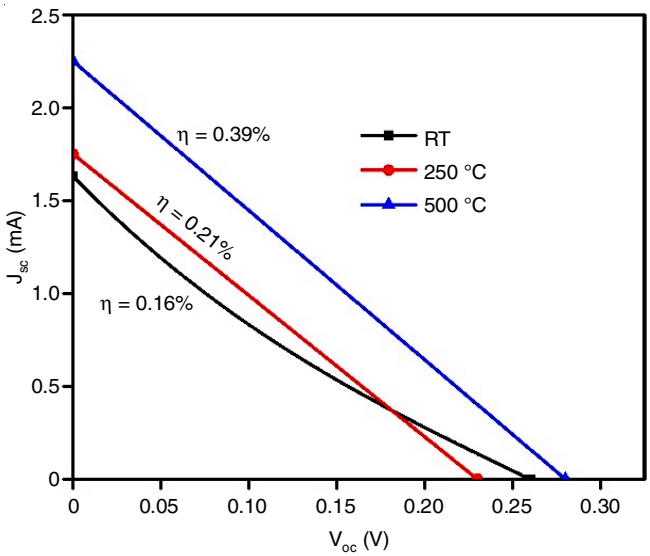

Fig. 6. V_{oc}-J_{sc} curve from experiment data of ATO thin film

The fill factor was calculated from eqn. 4:

$$\text{Fill factor (FF)} = \frac{P_m}{V_{oc} \times J_{sc}} \quad (4)$$

TABLE-3
PEC PARAMETERS OBTAINED FROM Sb DOPED SnO_2 FILMS

Condition of the thin film	I_{sc} (mA)	V_{oc} (V)	FF	η (%)	R_s (Ω)	R_{sh} (Ω)
Room temp. (without etching)	1.63	0.26	0.37	0.16	64	318
250 °C (without etching)	1.75	0.23	0.52	0.21	72	587
500 °C (without etching)	2.25	0.28	0.49	0.39	30	555

where P_m is the maximum power ($V_m \times I_m$).

Efficiency was calculated was calculated from eqn. 5:

$$\eta = \frac{J_{sc} \times V_{oc} \times FF}{P_{in}} \quad (5)$$

where P_{in} = 1000 W/m^2.

From the experimental data, the J_{sc} and V_{oc} were 1.63, 1.75 and 2.25 mA and 0.26, 0.23 and 0.28 V, respectively of the Sb-doped SnO_2 thin film at room temperature, 250 ºC and 500 ºC. The photocurrent efficiency increases with temperature at 500 ºC. This can be explained by the fact that controlled by different surface phenomena such as desorption and adsorption of O_2 due to the optimized temperature. The low efficiency of the cell may be due to the presence of surface states and grain boundaries that act as recombination centers for the photo-generated carriers [32]. The higher resistivity of the samples may also be attributed for the low efficiency.

Conclusion

An effective antimony-doped tin oxide (ATO) thin films successfully were prepared by thermal evaporation technique on ITO glass substrate. XRD analysis indicated that all films have polycrystalline tetragonal structure. The plot shows that the calcination temperature and particle size increased whereas effective strain decreased. SEM images also supported the XRD results and revealed the nanorod like features. The FTIR spectrum confirmed the formation of ATO. The optical band gap energy was calculated using Kubelka–Munk relation and the calculated values lie between 3.84 and 4.4 eV. The band gap energy shifted toward the bulk E_g value of SnO_2 (3.6 eV) when the calcination temperature increases. The UV emission at 362 nm in the photoluminescence spectrum, which indicates the suitability of SnO_2 for transparent conducting electrodes (TCOs).

CONFLICT OF INTEREST

The authors declare that there is no conflict of interests regarding the publication of this article.

REFERENCES

1. E. Shanthi, V. Dutta, A. Banerjee and K.L. Chopra, *J. Appl. Phys.*, **51**, 6243 (1980); https://doi.org/10.1063/1.327610
2. G. Jain and R. Kumar, *Opt. Mater.*, **26**, 27 (2004); https://doi.org/10.1016/j.optmat.2003.12.006
3. S. Shanthi, C. Subramanian and P. Ramasamy, *Cryst. Res. Technol.*, **34**, 1037 (1999); https://doi.org/10.1002/(SICI)1521-4079(199909)34:8<1037::AID-CRAT1037>3.0.CO;2-J
4. H. Kaneko and K. Miyake, *J. Appl. Phys.*, **53**, 3629 (1982); https://doi.org/10.1063/1.331144
5. K. Ravichandran and P. Philominathan, *Mater. Lett.*, **62**, 2980 (2008); https://doi.org/10.1016/j.matlet.2008.01.119
6. L. Lili, M. Liming and D. Xuechen, *Mater. Res. Bull.*, **41**, 541 (2006); https://doi.org/10.1016/j.materresbull.2005.09.011
7. J.-B. Han, H.-J. Zhou and Q.-Q. Wang, *Mater. Lett.*, **60**, 252 (2006); https://doi.org/10.1016/j.matlet.2005.08.032
8. J. Ma, Y. Wang, F. Ji, X. Yu and H. Ma, *Mater. Lett.*, **59**, 2142 (2005); https://doi.org/10.1016/j.matlet.2005.02.049.
9. K.y. Rajpure and C.H. Bhosale, *Mater. Chem. Phys.*, **63**, 263 (2000); https://doi.org/10.1016/S0254-0584(99)00233-3
10. Y. Hu, H. Zhang and H. Yang, *J. Alloys Compd.*, **453**, 292 (2008); https://doi.org/10.1016/j.jallcom.2006.11.062
11. J. Lee, *Thin Solid Films*, **516**, 1386 (2008); https://doi.org/10.1016/j.tsf.2007.05.027
12. M.R.S. Castro, P.W. Oliveira and H.K. Schmidt, *Semicond. Sci. Technol.*, **23**, 035013 (2008); https://doi.org/10.1088/0268-1242/23/3/035013
13. J.P. Coleman, J.J. Freeman, P. Madhukar and J.H. Wagenknecht, *Displays*, **20**, 145 (1999); https://doi.org/10.1016/S0141-9382(99)00016-5
14. Y.-H. Wong S. Cheng, K.Y. Chan and X.Y. Li, *J. Electrochem. Soc.*, **152**, D197 (2005); https://doi.org/10.1149/1.2041007
15. E.R. Leite, M.I.B. Bernardi, E. Longo, J.A. Varela and C.A. Paskocimas, *Thin Solid Films*, **449**, 67 (2004); https://doi.org/10.1016/j.tsf.2003.10.101
16. M. Acciarri, S. Binetti, A. Le Donne, B. Lorenzi, L. Caccamo, L. Miglio, R. Moneta, S. Marchionna and M. Meschia, *Cryst. Res. Technol.*, **46**, 871 (2011); https://doi.org/10.1002/crat.201000670
17. A.P. Rizzato, C.V. Santilli, S.H. Pulcinelli and A.F. Craievich, *J. Appl. Cryst.*, **36**, 736 (2003); https://doi.org/10.1107/S0021889803004953
18. R. Ramarajan, M. Kovendhan, K. Thangaraju, D.P. Joseph and R.R. Babu, *Appl. Surf. Sci.*, **487**, 1385 (2019); https://doi.org/10.1016/j.apsusc.2019.05.079
19. T.Y. Lim, C.Y. Kim, B.S. Kim, B.G. Choi and K. Shim, *J. Mater. Sci. Mater. Electron.*, **16**, 71 (2005); https://doi.org/10.1007/s10854-005-6453-4
20. T. Jintakosol, *Appl. Mechan. Mater.*, **749**, 141 (2015); https://doi.org/10.4028/www.scientific.net/AMM.749.141
21. L. Zhao, D.L. Zhang, G. Du, J.M. Xu and D.X. Zhou, *Mater. Trans. Tech.*, **280**, 831 (2005).
22. G. Bhatia, V.K. Gupta, M.M. Patidar, S.B. Srivasatava, D. Singh, M. Gangrade and V. Ganesan, *AIP Conf. Proc.*, **1953**, 100084 (2018); https://doi.org/10.1063/1.5033020
23. H. Kim and A. Pique, *Appl. Phys. Lett.*, **84**, 218 (2004); https://doi.org/10.1063/1.1639515
24. Y. Hu and S.H. Hou, *Mater. Chem. Phys.*, **86**, 21 (2004); https://doi.org/10.1016/j.matchemphys.2004.01.039
25. H.-R. An, C.Y. Kim, S.-T. Oh and H.-J. Ahn, *Ceram. Int.*, **40**, 385 (2014); https://doi.org/10.1016/j.ceramint.2013.06.013
26. V. Stambouli, M. Labeau, I. Matko, B. Chenevier, O. Renault, C. Guiducci, P. Chaudouët, H. Roussel, D. Nibkin and E. Dupuis, *Sens. Actuators B Chem.*, **113**, 1025 (2006); https://doi.org/10.1016/j.snb.2005.03.108
27. A.A. Alsac, A. Yildiz, T. Serin and N. Serin, *J. Appl. Phys.*, **113**, 063701 (2013); https://doi.org/10.1063/1.4790879
28. A. Ayeshamariam, C. Sanjeeviraja and R.P. Samy, *J. Photonics Spintronics*, **2**, 4 (2013).
29. G. Hodes, D. Cahen and J. Manassen, *Nature*, **260**, 312 (1976); https://doi.org/10.1038/260312a0
30. B.D. James, G.N. Baum, J. Perez and K.N. Baum, Technoeconomic Analysis of Photoelectrochemical (PEC) Hydrogen Production. DOE Contract Number: GS-10F-009J (2009).
31. W.W. Zhao, J.J. Xu and H.Y. Chen, *Anal. Chem.*, **90**, 615 (2018); https://doi.org/10.1021/acs.analchem.7b04672
32. K. Rajeshwar, *J. Appl. Electrochem.*, **25**, 1067 (1995); https://doi.org/10.1007/BF00242533